PNAS RESEARCH ARTICLE | PHYSICS

Light chaotic dynamics in the transformation from curved to flat surfaces

Chenni Xu[a,b], Itzhack Dana[a], Li-Gang Wang[b,1], and Patrick Sebbah[a,1]

Edited by Mordechai (Moti) Segev, Technion Israel Institute of Technology, Haifa, Israel; received July 9, 2021; accepted January 31, 2022

Light propagation on a two-dimensional curved surface embedded in a three-dimensional space has attracted increasing attention as an analog model of four-dimensional curved spacetime in the laboratory. Despite recent developments in modern cosmology on the dynamics and evolution of the universe, investigation of nonlinear dynamics of light on non-Euclidean geometry is still scarce, with fundamental questions, such as the effect of curvature on deterministic chaos, challenging to address. Here, we study classical and wave chaotic dynamics on a family of surfaces of revolution by considering its equivalent conformally transformed flat billiard, with nonuniform distribution of the refractive index. We prove rigorously that these two systems share the same dynamics. By exploring the Poincaré surface of section, the Lyapunov exponent, and the statistics of eigenmodes and eigenfrequency spectrum in the transformed inhomogeneous table billiard, we find that the degree of chaos is fully controlled by a single, curvature-related geometric parameter of the curved surface. A simple interpretation of our findings in transformed billiards, the "fictitious force," allows us to extend our prediction to other classes of curved surfaces. This powerful analogy between two a priori unrelated systems not only brings forward an approach to control the degree of chaos, but also provides potentialities for further studies and applications in various fields, such as billiards design, optical fibers, or laser microcavities.

chaos | curved space | transformation optics

Significance

Exploring light dynamics and chaos on curved surfaces is one of the new challenges met in modern cosmology. To address this question and investigate chaotic dynamics of light on three-dimensional curved surfaces, we consider their connection under a conformal transformation with flat billiards with spatially varying refractive index. Through this connection, we demonstrate that these two systems share the same dynamics; the complexity of the problem simplifies, and well-known tools originating from chaos analysis in planar billiards can be used to explore chaotic dynamics on curved space. We discover that the degree of chaos is fully controlled by a single curvature-related geometrical parameter, providing a degree of freedom in chaos engineering, as well as potentialities to design nonuniform table billiards/cavities/resonators.

1. Introduction

Einstein's general theory of relativity (GR) unprecedentedly interprets gravity in a geometrical framework; namely, the presence of a massive object distorts the very fabric of the space and time in its vicinity. Despite GR's triumph, gravitational effects are, in principle, too feeble for light to be perceived in a laboratory environment. One of the analog models of GR is two-dimensional (2D) curved surfaces embedded in three-dimensional (3D) space, whose theoretical cornerstones are the 3+1 membrane paradigm (1) and embedding diagrams. After taking a constant time and extracting the equatorial slice of a spherically symmetrical space, the remnant metric can be visualized through a 2D curved surface. Ever since this innovative notion was brought up by Batz and Peschel (2), electromagnetic (EM) dynamics and wave propagation on 2D curved surfaces have been prosperously developed both theoretically (3–10) and experimentally (11–15). On the other hand, GR notions could reciprocally contribute to the engineering of nanophotonic devices (15, 16) and transformation optical designs, ranging from EM invisible cloaks (17, 18) to perfectly focusing lenses (19–21), based on manipulation of the curved geodesic paths.

Investigation of nonlinear dynamics in the context of GR may date back to the 1960s and has been extensively discussed in various aspects (22–24). Nonlinear dynamics, or chaos, widely exists in diverse modern scientific disciplines. One characteristic of chaos is the exponential sensitivity to initial conditions, with a well-publicized metaphor being the "butterfly effect." In the recent decades, instead of being considered a nuisance, wave chaos has been taken advantage of to ameliorate optical resonators and laser microcavities (25–34), such as enhancing energy storage (25), suppressing spatiotemporal lasing instabilities (26), realizing high-power directional emission (27–29), etc. To this end, information about dynamical behaviors in a 2D cavity, such as critical periodic orbits (POs) and the volume of chaotic area in phase space, is significant. One paradigm model is a 2D table (or flat) billiard, which is typically a closed domain, wherein particles and light rays propagate freely, except for elastic collisions on its boundaries. Various degrees of chaos in table billiards are realized by either deforming the boundaries (35–37) or introducing external force (38–40). In a recent work, a novel notion, a transformed cavity, is proposed with a nonuniform profile of a refractive index present in a deformed optical cavity (41). Such a transformed cavity opens up a new pathway of chaos engineering.

Author contributions: C.X., I.D., L.-G.W., and P.S. designed research; C.X. performed research; C.X., I.D., L.-G.W., and P.S. analyzed data; and C.X., L.-G.W., and P.S. wrote the paper.

The authors declare no competing interest.

This article is a PNAS Direct Submission.

[1]To whom correspondence may be addressed. Email: patrick.sebbah@biu.ac.il or lgwang@zju.edu.cn.

This article contains supporting information online at https://www.pnas.org/lookup/suppl/doi:10.1073/pnas.2112052119/-/DCSupplemental.

Published March 16, 2022.

Fundamental questions arise in the investigation of light chaotic dynamics on a non-Euclidean geometry, among them the role of curvature, a new degree of freedom that is not present in flat space. Yet, challenges exist, including the complexity of the equations induced by the curved geometry, as well as the ambiguity of concepts, such as the definition of boundaries and indicators of chaos. To the best of our knowledge, the wave-chaos idea has been carried over in a few curved elastic systems (42–44), such as aluminum thin shells (42), yet has rarely been explored in optics, except for a very recent study about ray chaotic behavior on a deformed toroidal surface (45). Here, we address this challenge by considering the analogy between a curved surface and a 2D table billiard with nonuniform distribution of the refractive index, on the strength of transformation optics (TO). The mathematical underpinning of TO is the form invariance of Maxwell equations under general coordinate transformation, with the optical constitutive parameters of the transformed media (i.e., engineering the permittivity ε and permeability μ tensor explicitly) (46, 47). As we will demonstrate, this approach of projection provides a possibility to utilize physical systems on one surface to explore their counterparts on the other, especially when the studies in one of the systems are demanding to carry on.

In this work, we study classical and wave chaos on a special type of 2D curved surfaces in 3D space, surfaces of revolution (SORs), by investigating light propagation in its corresponding table billiard with azimuthally symmetric nonuniform distribution of refractive index. We exemplarily choose a typical family of SORs, the Tannery surfaces. Since such surfaces are integrable, we consider half of the surface and its 2D nonuniform billiard, where a circular hole is pierced to introduce chaos. We prove rigorously that these two systems share the same dynamics by showing that a conformal coordinate transformation preserves both geodesic equations and wave equations. Utilizing this equivalence, we can assess the degree of chaos in one system (the curved surface) by probing the nature of the trajectories in Poincaré surface of section (SOS) and measuring the Lyapunov exponent in the other (the flat billiard). We find that the degree of chaos is fully controlled by a single geometrical curvature-related parameter of the Tannery surface. This is also revealed in the statistics of eigenmodes of the Tannery surfaces, as the wave equation is invariant for both systems. At last, we show that the above results can be generalized to arbitrary SORs, by coming up with a universal quantity in the 2D nonuniform billiards. This simple interpretation further demonstrates the potentialities of our approach.

2. Results

2.1. Basic Theory. As its name indicates, an SOR can be generated by revolving an arbitrary plane curve (known as a generatrix) around an axis of symmetry for a circle. The line element of a typical SOR takes the form $ds^2 = g_{\alpha\beta}dx^\alpha dx^\beta = E(u)du^2 + G(u)dv^2$, with u along longitudinal direction and v, being the rotational angle, along transverse direction, as shown in Fig. 1*A*. In curved spaces, light rays propagate along geodesics, in analogy with straight lines in free space. On the basis of geodesic equations, an arbitrary geodesic with given initial conditions is depicted by (for mathematical details, see *SI Appendix*, section 1)

$$dv = \eta \frac{\kappa\sqrt{E(u)}}{G(u)\sqrt{1-\frac{\kappa^2}{G(u)}}}du. \qquad [1]$$

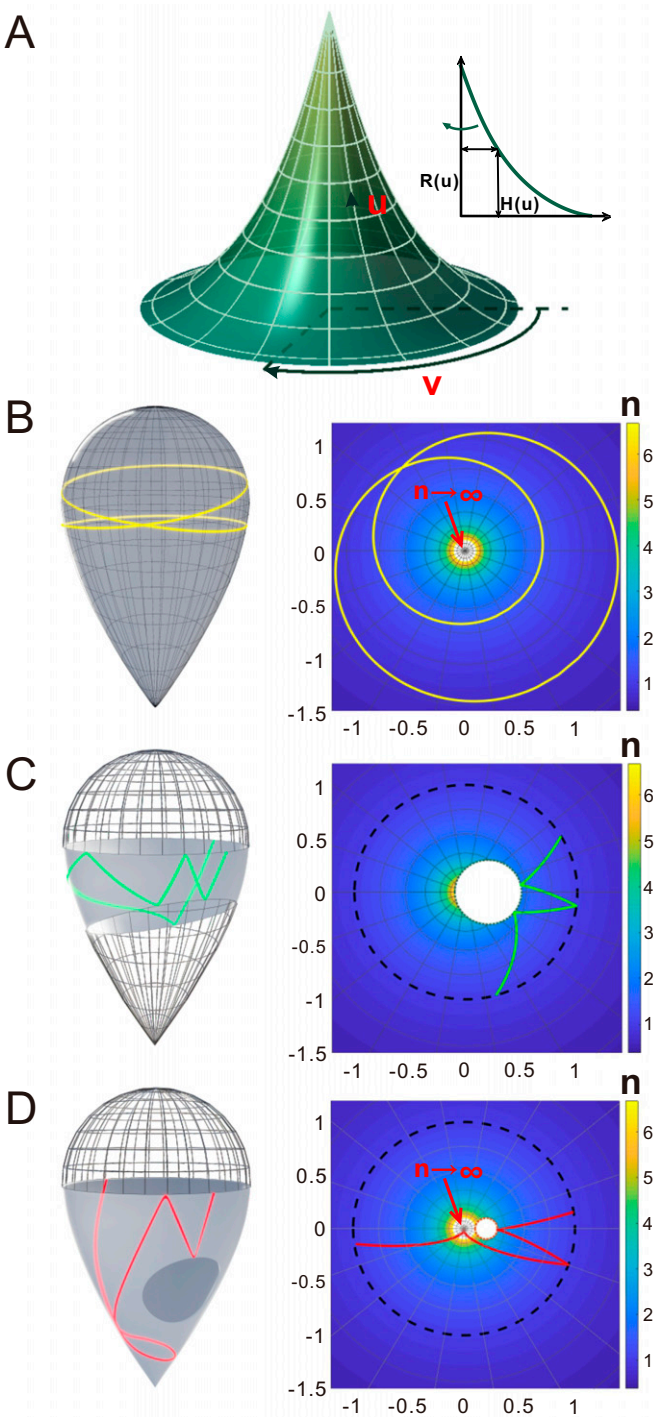

Fig. 1. (*A*) Sketch of a typical SOR with the orthogonal curvilinear coordinates on it. *A*, *Inset* illustrates its generatrix. (*B*) Tannery surface with $c = 2$ (*Left*) and its projected billiard (*Right*). A typical closed trajectory is depicted by the yellow solid line. (*C* and *D*) Truncated Tannery surfaces that have a circular hole with radius 0.3 (dark green dotted line) (*C*) and radius 0.1 (orange dotted line) (*D*) in their projected billiards. The equators are denoted by black dashed lines in the projected billiards. Two typical trajectories are plotted by green and red solid lines, respectively.

Here, $\eta = \mathrm{sgn}\left[(du/ds)_{\mathrm{initial}}\right]$ is determined by the initial direction, and slant κ, defined as $\left[G(u)dv/ds\right]_{\mathrm{initial}}$, remains invariant as a consequence of the conservation of angular momentum (9). When it comes to waves, the time-harmonic scalar EM field follows the massless Klein–Gordon equation

$$\frac{1}{\sqrt{E(u)G(u)}}\frac{\partial}{\partial u}\left[\sqrt{\frac{G(u)}{E(u)}}\frac{\partial\Phi}{\partial u}\right]+\frac{1}{G(u)}\frac{\partial^2\Phi}{\partial v^2}+k^2\Phi=0, \quad [2]$$

with k being the propagation constant.*

In this work, instead of directly investigating light propagation on the surface, we employ an alternative method by projecting an SOR onto a plane with distribution of refractive index, in light of conformal TO (48, 49). This notion is mathematically underlain by the theorem that any 2D Riemannian manifold is conformally flat. Namely, the metric of an arbitrary 2D curved surface ds^2 can be conformally related to the metric of a flat plane ds_{f}^2 through $ds^2=\Lambda ds_{\mathrm{f}}^2$, where Λ is a differentiable function (50). Interestingly, the right-hand side, defined as ds'^2, perfectly describes an inhomogeneous planar dielectric medium with spatially varying refractive index $n=\sqrt{\Lambda}$. For SORs, thanks to their rotational symmetry, we can naturally suppose that the projected plane is azimuthally symmetric. Consequently, the polar coordinate is chosen out of convenience, and the variation of refractive index rests exclusively on the radial component. Based on the premise that $ds^2=ds'^2$, an equivalence between these two systems can be established through the coordinate mapping (51)

$$r(u)=A\exp\left[\int^u\sqrt{\frac{E(u')}{G(u')}}du'\right],\ \varphi=v, \quad [3]$$

with distribution of refractive index

$$n(u)=\frac{\sqrt{G(u)}}{A}\exp\left[-\int^u\sqrt{\frac{E(u')}{G(u')}}du'\right]. \quad [4]$$

Here, A is a positive integration constant, and r and φ are radial and azimuth coordinates on the plane.

By virtue of this coordinate mapping, the transformed version of Eq. **1** appears as

$$d\varphi=\eta'\frac{\kappa'}{n(r)r^2\sqrt{1-\frac{\kappa'^2}{n^2(r)r^2}}}dr, \quad [5]$$

with $\eta'=\mathrm{sgn}\left[(dr/ds')_{\mathrm{initial}}\right]$ and $\kappa'=\left[n^2(r)r^2d\varphi/ds'\right]_{\mathrm{initial}}$. We prove in *SI Appendix*, section 2 that Eq. **5** is the very solution of geodesic equations on the projected plane. Thus, the dynamics of light rays are preserved in both systems. In terms of waves, Eq. **2** is transformed into

$$\frac{1}{r}\frac{\partial}{\partial r}\left(r\frac{\partial\Phi}{\partial r}\right)+\frac{1}{r^2}\frac{\partial^2\Phi}{\partial\varphi^2}+k^2n^2(r)\Phi=0, \quad [6]$$

which is exactly the wave equation of electric field on a plane with distribution of azimuthally symmetric refractive index $n(r)$. As a result, the transformation preserves the solutions of wave equation in one system to be the eigenmodes of the other. In *SI Appendix*, section 2, we generalize this result to arbitrary coordinate transformation. This demonstrates that light dynamics completely parallel in both systems. With this dynamical equivalence, we can safely investigate one system to infer about the other.

When an SOR is closed (e.g., a sphere or spindle) or infinitely extends (e.g., a cylinder or cone), its projection covers the whole plane. A paradigmatic example is the so-called "Tannery surfaces," which is an object of interest for mathematicians (52) and is going to be the study case of this paper. The family of Tannery surfaces can be parameterized by $E(u)=(c+\cos u)^2$, $G(u)=\sin^2 u$,† with c being a positive constant and, in the meantime, the single parameter to depict this family of surfaces (for the description of Tannery surfaces embedded in the Cartesian and cylindrical coordinate system, see *SI Appendix*, section 1). It is proved that such surfaces have a constant period function $2c\pi$ (53). That is, when the parameter c is an integer, all the geodesics (except the ones along longitudinal u direction) are closed, and for a particle that departs from an arbitrary position on the geodesic moves along it and returns to the starting point, the accumulated variation in coordinate v is $2c\pi$, as shown in Fig. 1*B*. In order to limit our study to a finite area on plane, a mirror is put on the "equator" (i.e., the latitude with $u=\pi/2$; black dashed lines in Fig. 1 *C* and *D*) of the surface, which plays the role of a perfectly reflecting boundary, and only the lower half of the surface is taken. On the projected plane, the equator corresponds to a circle with radius r_{B}, while the lower half of the surface corresponds to the area inside the circle, which together naturally form a circular billiard. In what follows, coordinate r will be normalized by r_{B}, resulting in the billiard being unit-sized (as shown in the right column of Fig. 1 *C* and *D*) and subsequent analyses being dimensionless. These two systems are absolutely integrable since the number of constants of motion (energy and orbital angular momentum) is equal to the dimensionality of the system (54), owing to the rotational symmetry of SORs. To introduce chaos in this system, an off-centered, disk-shaped area is eliminated, leaving a circular hole with a specular boundary in the billiard. The choice of a disk shape is out of consideration of simpleness, yet more complex shapes could be explored. The right column of Fig. 1 *C* and *D* shows two typical holes, whose centers are located at 0.2 (in unit of radius) from the centers of the billiards and whose radii are 0.3 and 0.1, denoted by dark green and orange dotted lines, respectively. By taking the coordinate transformation Eq. **3**, the correspondence of these two holes on the surface are shown in the left column. It is seen that the refractive index approaches to infinity at the center of the projected billiard, corresponding to the apex of the surface in the bottom, which is basically a singularity for light rays. We focus in the rest of the paper on the cases where the hole includes the billiard center, resulting in the removal of the bottom apex. Its correspondence on the surface is a boundary unparallel to latitudes, rather than a hole.

In what follows, in order to distinguish them from their 2D projected billiards, SORs are referred to as "3D surfaces," based on the fact that they are embedded in 3D space, despite being 2D per se. Besides, unless otherwise specified, the off-centered disk will be eliminated in the fashion of Fig. 1*C*.

2.2. Poincaré SOS. Classical chaotic signatures are, in principle, derived from classical mechanics and, in our context, light ray pictures. Unlike finite beams, light rays are exclusively defined by their positions and directions, from which their geodesic trajectories are determined. Ray trajectories become rapidly intractable in real space after a few bounces; it is therefore more advisable to inspect ray motions in phase space, which are composed of two spatial dimensions and their conjugate momenta. For billiard

*The precise evolution of vector light fields is described in section II of ref. 2, starting from 3D Maxwell equations written in general coordinates. Specifically, for EM wave polarizing strictly along the transverse direction, its wave equation also takes the form of Eq. **2**, except for an extra curvature-induced potential, whose effect is discussed in ref. 8.

†More precisely, the parameterization of Tannery surfaces is $E(u)=a^2(c+\cos u)^2$, $G(u)=a^2\sin^2 u$, where a is a constant with unit of length governing the size of the surface. From what is demonstrated in *SI Appendix*, section 6, the size of the surface does not affect the results presented in this work. Therefore in what follows, a is taken as 1 m without loss of generality.

systems, an effective approach to extract information from four-dimensional phase space is to record the states of the trajectory only when it collides on the outer boundary. This 2D section of phase space is known as the Poincaré SOS and is conveniently depicted in the framework of the Birkhoff coordinate, as sketched in Fig. 2 *A*, *1*. In practice, the trajectories between two bounces are traced by Eq. **1**. When the trajectories collide on the hole/lower unparallel boundary, the rule of specular reflection is applied in the 2D projected billiard, after projecting the trajectories on the 3D surface back to the inhomogeneous plane. This step saves one from complicated or even impracticable calculation on the 3D surface since the analytical expression of the lower unparallel boundary is inaccessible.

When $|\sin\chi|$ is large enough, trajectories propagate near the outer boundary of the 2D projected billiard/equator of 3D surface and are therefore free from colliding on the hole/lower unparallel boundary. Their tangential momenta $|\sin\chi|$ remain invariant, so that in Poincaré SOS, these trajectories are represented by horizontal straight lines. In contrast, trajectories with small $|\sin\chi|$ collide on the hole/lower unparallel boundary, resulting in their representations ergodically and irregularly distributed in the central part of Poincaré SOS, which therefore forms a chaotic sea. Among these trajectories, some return to their initial conditions after several bounces and retrace themselves repeatedly. Such POs are represented as a succession of points in SOS, with the number of points equal to the number of bounces on the outer boundary/equator in each period. For some POs, the trajectories whose initial conditions are slightly deviated from the critical conditions of POs are able to survive in the vicinity of the latter. Such POs, considered as stable POs, form regular islands among the chaotic sea in Poincaré SOS together with their quasi-periodic orbits. As a contrast, the other unstable POs are submerged in the chaotic sea and can be scarcely recognized. Some typical stable and unstable POs are illustrated by diamonds and pentagrams, respectively, in Fig. 2 *A*, *2*, *B*, *2*, *C*, *2*, and *D*, *2*, and the corresponding trajectories in the billiards are depicted in Fig. 2 *A*, *3*, *B*, *3*, *C*, *3*, and *D*, *3* with the same labels and colors. An interesting feature of PO with label #1 is explicated in *SI Appendix*, section 3.

A generic presentation about the Poincaré SOSs of four typical Tannery surfaces with $c = 0$, 1, 2, and 5 is given in Fig. 2. Different shapes of the surfaces are clearly exhibited in Fig. 2 *B*, *1*, *C*, *1*, and *D*, *1*. Specially, when $c = 0$, the metric of the surface degenerates to $ds^2 = \cos^2 u du^2 + \sin^2 u dv^2$, which is equivalent to a polar coordinate if one takes $\sin u$ as the radial component and v as the azimuth component. Thus, surface with $c = 0$ corresponds to the flat billiard and serves as a reference. The Poincaré SOSs reveal that the phase spaces of all the four surfaces are mixed, with coexistence of both regular and chaotic trajectories. One can observe that the area of chaotic sea remarkably enlarges with the parameter c, implying an increasingly chaotic phase-space structure of Tannery surface with greater parameter c. Another phenomenon one may meanwhile notice is an obvious reduction in the amount of stable POs and the area of islands, especially in Fig. 2 *B*, *2*, *C*, *2*, and *D*, *2*. These two hints suggest an increasing proportion of trajectories transferring from regular to chaotic and, consequently, indicate a more significant degree of chaos. Note that this observation is true both on the 3D surface and in the 2D billiard with refractive index landscape because of their equivalence.

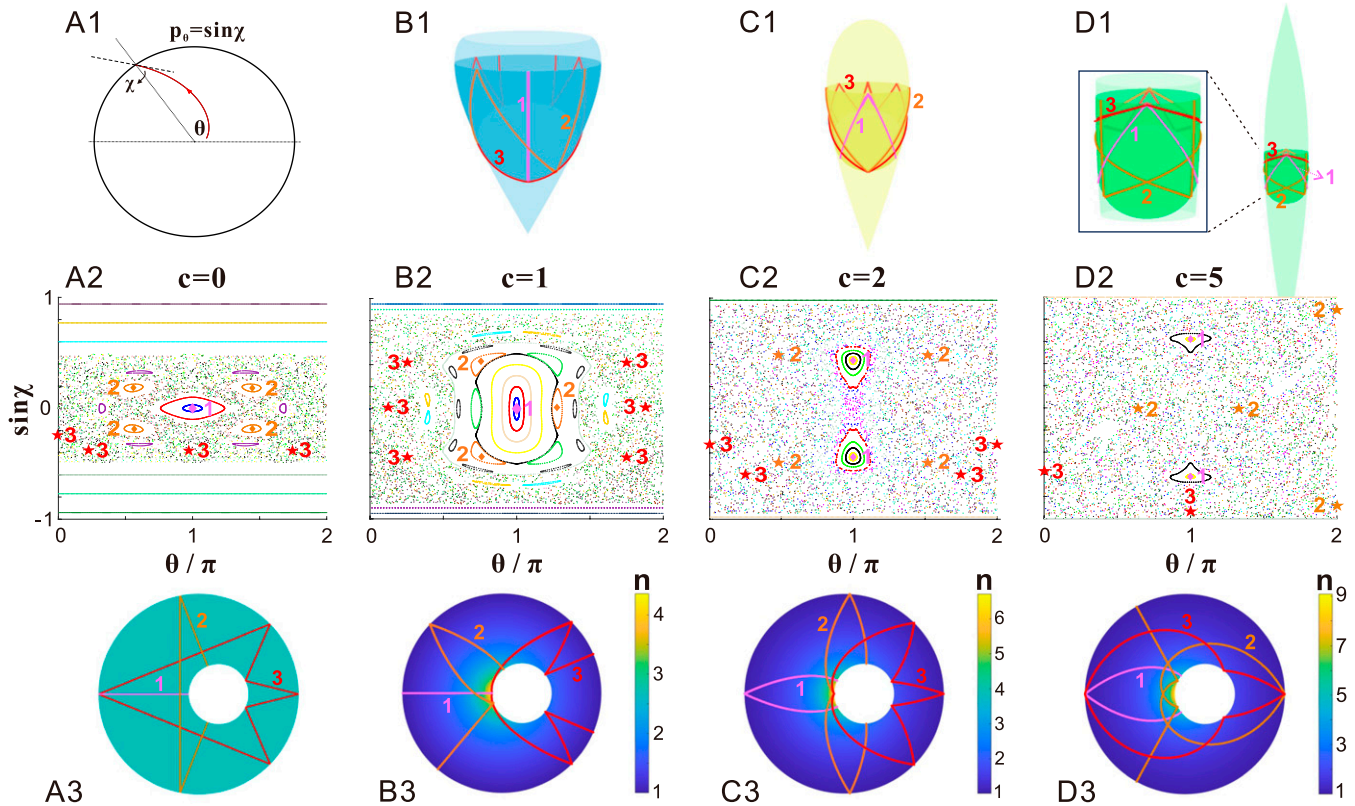

Fig. 2. Poincaré surfaces of section of Tannery surfaces with different parameter c. (*A*, *1*) Sketch of Birkhoff coordinates. (*B*, *1*, *C*, *1*, and *D*, *1*) Sketches of Tannery surfaces with $c = 1$, 2, and 5, respectively. The transparent parts correspond to areas outside the projected billiard and inside the hole, which are excluded in the study. (*A*, *2*, *B*, *2*, *C*, *2*, and *D*, *2*) Poincaré surfaces of sections of Tannery surfaces with $c = 0$, 1, 2, and 5, respectively. Each color represents an arbitrary trajectory. The diamonds and pentagrams, respectively, indicate typical stable and unstable POs, whose representations in Poincaré SOS are a succession of points. These POs in real space are exhibited in *A*, *3*, *B*, *3*, *C*, *3*, and *D*, *3*, respectively, corresponding to the points with the same label and color.

2.3. Lyapunov Exponent. As was mentioned, a hallmark of chaos is the sensitivity to initial conditions, i.e., the exponential divergence of two extremely nearby trajectories in phase space. The speed of this exponential divergence is characterized by the (maximum) Lyapunov exponent λ. Here, we adopt the method of the "billiard map" in terms of the collisions of trajectories on the outer boundary, instead of the "billiard flow" with continuous time (55). In this way, the Lyapunov exponent is defined as

$$\lambda = \lim_{N\to\infty} \frac{1}{N} \sum_{i=1}^{N} \ln \frac{|\boldsymbol{\delta}_i|}{|\boldsymbol{\delta}_0|}, \qquad [7]$$

where $|\boldsymbol{\delta}_i|$ is the distance of the two chosen trajectories in phase space at the ith bounce. In practice, two sets of extremely close initial conditions are randomly chosen from the chaotic area in Poincaré SOS, and distance $|\boldsymbol{\delta}|$ is collected every time two trajectories collide on the outer boundary. Theoretically, if the number of bounces N is large enough, Eq. **7** is supposed to approach to a constant that is independent of the choice of initial conditions. Technical details about the calculation of Lyapunov exponents are specified in *SI Appendix*, section 4.

By this method, Lyapunov exponents of a series of Tannery surfaces with varying parameter c and under three different means of truncation are calculated and illustrated in Fig. 3*A*. Each data point in Fig. 3*A* is the result of averaging over four to six randomly chosen pairs of trajectories, where each pair of trajectories experiences several tens of thousands of bounces on the outer boundary/equator, and an approximate convergence has been reached (an example of five typical pairs of trajectories is shown in Fig. 3*B*). The figure manifests an overall increasing tendency of Lyapunov exponents with increasing parameter c of Tannery surfaces, indicating that, in general, when parameter c increases, the speed of divergence between two close trajectories, or the instability of the trajectories, increases, which validates the increase of degree of chaos both on the 3D surface and in the 2D projected billiard. Furthermore, the invariance of this increasing tendency, despite different positions and radii of the pierced hole in the projected billiard, attests to the universality of this feature, as shown in Fig. 3*A*. Compared with the qualitative interpretation obtained from Poincaré SOS with a coarse sampling of parameter c, this signature brings a more quantitative insight, which enables a finer exploration and hence reveals more details about the dependence of chaoticity on parameter c. One example is that an exception to this increasing trend is observed near $c = 1$, elucidating that the variation of chaoticity with parameter c is not strictly monotonous.

2.4. Statistics of Eigenmodes and Eigenfrequency Spectrum. When it comes to quantum or wave realm, notions of phase space and trajectories are not properly defined due to the uncertainty principle. Therefore, signatures in classical chaos are no longer valid, but are replaced by quantum mechanical criteria based on the energy spectrum, energy eigenvectors, entanglement, temporal evolution of expectation values, etc. In this section, we are going to focus on the first two fingerprints.

We have demonstrated that the wave equation on an SOR is identical to that in its projected billiard, bridged by the coordinate transformation. Namely, the performed calculation, as well as the concepts and phenomena in one system, can be automatically extended to the other. Here, we obtain eigenmodes in both systems with the help of COMSOL Multiphysics 5.2. In practice, the simulation is conducted in the 2D inhomogeneous billiard because of the difficulty in constructing a 3D surface (especially when the expression of the lower unparallel

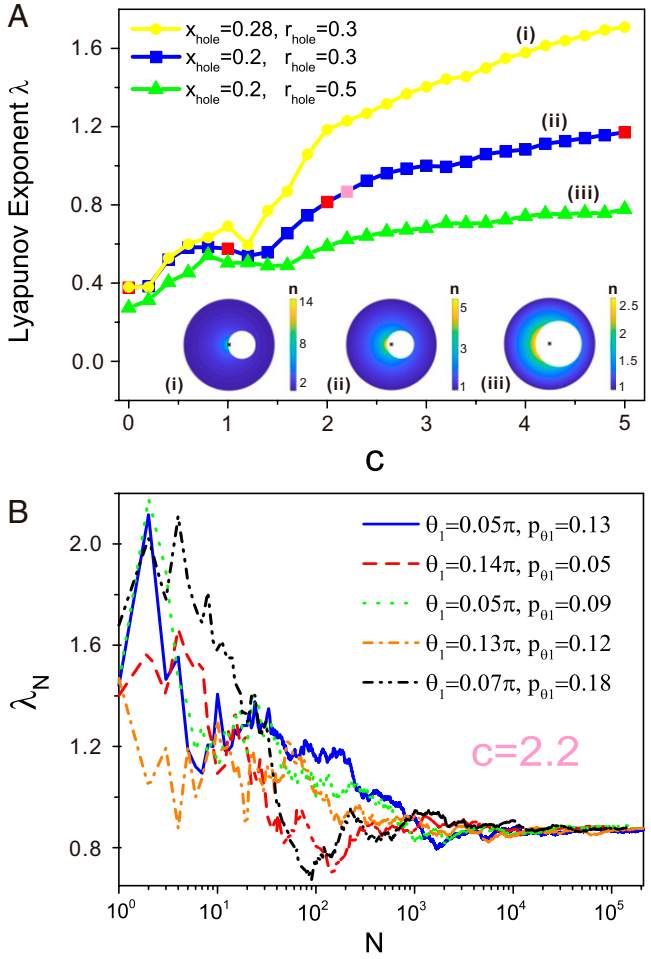

Fig. 3. (*A*) Variation of Lyapunov exponents versus the parameter c of Tannery surfaces and three different means of truncation. The distribution of the refractive index are illustrated in *A*, *Inset* with corresponding labels, and the black cross denotes the center of the billiard. The red square data markers in line *ii* correspond to the cases illustrated in Fig. 2. (*B*) The quantity λ_N at *N*th bounce, calculated by Eq. **7**. Five pairs of extremely close trajectories are randomly chosen at the case denoted by the pink square data marker in *A*, whose initial conditions are shown in the legend with $\theta_2 = \theta_1 + 10^{-4}$, $p_{\theta_2} = p_{\theta_1} + 10^{-4}$. All five pairs of trajectories converge to the same asymptotic value, which is defined as a Lyapunov exponent.

boundary is unknown), and the eigenfunction on the 3D surface is subsequently obtained by projection from the 2D billiard via the coordinate transformation. Here, for the sake of consistency, we define dimensionless eigenfrequency $\tilde{\omega}_i = \omega_i r_B / c_L$ from the simulated eigenfrequency spectrum $\{\omega_i\}$, where c_L is the speed of light. Three typical eigenmodes in both systems are illustrated in *SI Appendix*, Fig. S5.

One credible imprint of ray chaos resides in the spatial statistics of eigenmodes (56). To be specific, the wave function of a typical ergodic eigenmode, whose classical correspondence has a stochastic motion, distributes uniformly over the whole available area of the phase space, which is ergodically visited by its classical trajectories. Such modes are thus conjectured as a random superposition of plane waves with different amplitudes, phases, and directions, but the same wavenumber, manifesting an analogous pattern of laser speckles. As per the central limit theorem, such a field is Gaussian random, implying that the amplitude of eigenmode follows the Gaussian statistical distribution

$$P(\Phi) = \frac{1}{\sqrt{2\pi \langle \Phi \rangle}} \exp\left(-\frac{\Phi^2}{2\langle \Phi \rangle}\right), \qquad [8]$$

while the probability distribution of intensity $I = \Phi^2$ is subjected to

$$P(I) = \frac{1}{\sqrt{2\pi I / \langle I \rangle}} \exp\left(-\frac{I}{2\langle I \rangle}\right), \quad [9]$$

known as Porter–Thomas (PT) distribution. Fig. 4 *A* and *B* illustrate a typical ergodic eigenmode of truncated Tannery surface with $c = 1$, both on the 3D surface and the 2D projected plane. The good agreement of its $P(\Phi)$ and $P(I)$ with Gaussian and PT distribution, respectively, validates the ergodicity of the eigenmode.

Besides ergodic modes with speckle statistics, there exists a special class of modes with enhanced amplitude in the vicinity of single unstable POs in the corresponding classical system. This ubiquitous, yet remarkable, phenomenon is well known as quantum scarring (57). Unlike the enhancement of eigenstate intensity near stable POs, which are well understood by the semiclassical theory of integrable systems, scar was initially an unexpected phenomenon and was later found to be a significant correction to predictions from random matrix theory and Gutzwiller trace formula. One of the scarred modes of truncated Tannery surface with $c = 1$ on projected plane and 3D surface is exhibited in Fig. 4 *E* and *F*, superimposed by a white solid line indicating its corresponding unstable PO. A prominent deviation of $P(\Phi)$ and $P(I)$ from ergodicity can be clearly observed in Fig. 4 *G* and *H*, respectively.

Another classic and widely recognized indicator for the randomness of a quantum system is the distribution of nearest-neighbor spacing (NNS) of the eigenfrequency spectrum (58). In a classically integrable system, successive eigenfrequency distributes randomly, and the NNS s follows the Poisson law

$$P_{\text{Poisson}}(s) = \exp(-s), \quad [10]$$

with its peak located at zero. While in classically chaotic systems, the presence of level repulsion leads NNS to best-fit Wigner–Dyson (WD) distribution

$$P_{\text{WD}}(s) = \frac{\pi s}{2} \exp\left(-\frac{\pi}{4} s^2\right). \quad [11]$$

In contrast with Poisson distribution, where level spacing can be zero with the highest probability, a salient consequence of level

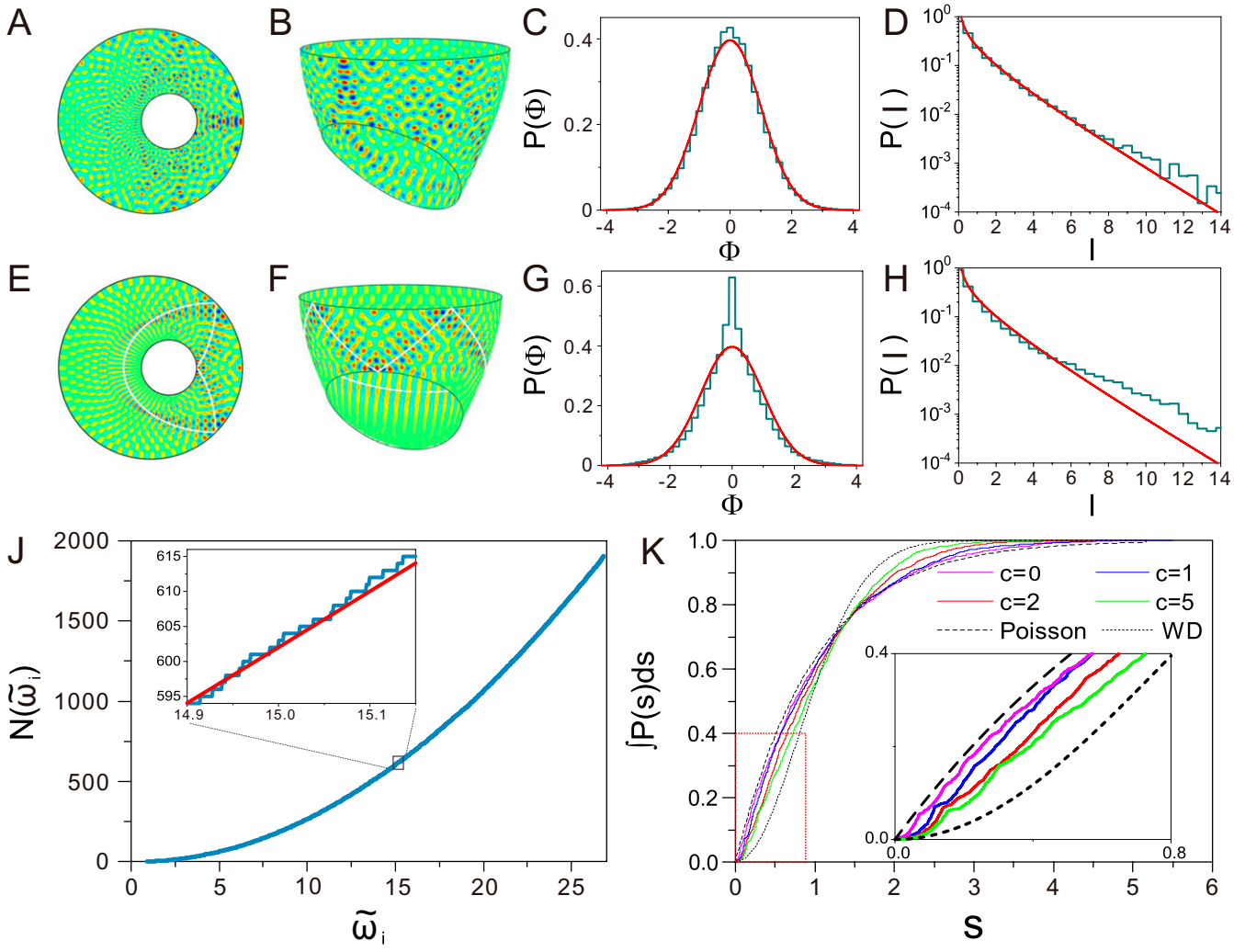

Fig. 4. (*A–H*) Spatial statistics of eigenmodes. (*A* and *B*) The field distributions (amplitude) of a typical ergodic eigenmode (with dimensionless eigenfrequency $\tilde{\omega} = 29.639$) of truncated Tannery surface with $c = 1$ in the projected billiard (*A*) and on the 3D surface (*B*). Its distribution of amplitude and intensity are plotted in *C* and *D*, respectively, with the red solid line being Gaussian and the PT distribution as reference. The field distributions (amplitude) of a typical scarring eigenmode (with dimensionless eigenfrequency $\tilde{\omega} = 28.863$) and their statistics are shown in *E–H*. The white solid lines in *E* and *F* indicate its corresponding unstable PO. (*J* and *K*) Statistics of the eigenfrequency spectrum. (*J*) Cumulative eigenfrequency density $N(\tilde{\omega}_i)$ of the Tannery surface with $c = 2$ versus dimensionless eigenfrequency $\{\tilde{\omega}_i\}$. (*K*) Distribution of the NNS of Tannery surfaces with $c = 0$ (purple), 1 (blue), 2 (red), and 5 (green). The Poisson (black dashed) and WD (black short dashed) distribution are also plotted as reference. (*J, Inset, and K, Inset*) Zoom-in of the areas marked by the black and red dotted rectangles, respectively.

repulsion is the vanishment of infinitesimal NNS, i.e., $P(s) \to 0$ when $s \to 0$. This behavior can be well explained by the Bohigas–Giannoni–Schmit conjecture (59) that spectra of time-reversal-invariant systems reveal the same fluctuation properties as a Gaussian orthogonal ensemble in random matrix theory. When the system has mixed dynamics, its distribution of NNS is intermediate between the two limiting cases. In virtue of COMSOL Multiphysics 5.2, we also got access to the eigenfrequency spectra and consequently performed an unfolding procedure (for more details, see *SI Appendix*, section 5). The resulting distributions of NNS of truncated Tannery surfaces with $c = 0, 1, 2, 5$ are plotted in Fig. 4*K*. In order to eliminate the effect of an artificially chosen interval on the distribution curve, we adopt the cumulative distribution instead of widely used histogrammic representation. One can clearly observe that distributions of NNS of all four cases interpolate between Poisson and WD distributions, indicating that these surfaces are mixing systems. Comparing the distributions of the four cases, especially in the range of small spacing s, which is zoomed-in in Fig. 4 *K*, *Inset*, the distribution curves gradually deviate from a Poisson distribution and incline to a WD distribution with the increase of parameter c, manifesting a tendency of increasing chaoticity.

3. Discussion

The above-mentioned three signatures explicitly demonstrate an increasing tendency of chaoticity with the geometrical parameter c. In this section, we propose a qualitative interpretation on this phenomenon. One should note that it is the unparallel lower boundary on the 3D surface/hole in the projected billiard, or, namely, the breaking of symmetry, that gives birth to the chaotic dynamics in the first place (60). On this basis, the presence of a curved surface further alters the chaoticity. There are two parallel approaches to conduct the analysis, either on 3D surfaces or in 2D projected billiards. When considering from the perspective of 3D surfaces, on different SORs, trajectories follow their respective geodesics, the undisturbed natural paths. Yet, the lower unparallel boundaries, which are the reciprocal projection of the hole in the projected billiards, have different shapes, leading to different degrees of chaos (for details, see *SI Appendix*, Fig. S4, as well as our discussion in *SI Appendix*, section 4). However, the various properties of surfaces, such as the expression of generatrix, curvature, etc., could perplex the discussion. Whereas after being projected onto a plane, all the information relevant to chaotic dynamics is completely and merely embodied in the distribution of reflective index (since the location and radius of the hole are fixed in all projected billiards with varying c), which simplifies the problem to a great extent. Fig. 5*A* compares trajectories with identical initial conditions in the projected billiards of Tannery surfaces with parameter $c = 0, 1, 2, 5$. One can observe visually that with the presence of the nonuniform refractive index, the trajectories deflect toward the center of the billiard, as if they were subjected to a "fictitious force." More importantly, in the projected billiard with greater parameter c, the trajectories experience more conspicuous deflections, enhancing the chance of collision on the hole. Put in another way, a greater initial tangential momentum p_θ is required to realize the whispering gallery orbits, resulting in a larger area of chaotic sea and consequently a greater chaoticity of the system. We surmise that the degree of deflection is proportional to the rate of variation of the refractive index and hypothetically quantify the fictitious force to be

$$\boldsymbol{\mu} = \frac{r}{n(r)} \nabla n(r), \qquad [12]$$

with r being the radial coordinate and $n(r)$ being the refractive index profile. Details about construction of Eq. **12** are revealed in *SI Appendix*, section 6. Owing to the azimuthal symmetry of SORs, $\boldsymbol{\mu}$ is along the radial direction. Further calculation shows that the magnitude of $\boldsymbol{\mu}$ is determined uniquely by the metric of the surface (*SI Appendix*, section 7). Besides, one may observe that the term in the absolute value sign is always negative, indicating that in the projected billiards of any SORs, the fictitious force always points toward the center of the billiard. Fig. 5*B* illustrates the increasing trend of $|\boldsymbol{\mu}(r)|$ with parameter c, which coincides with our assumption. Our interpretation is supported by Fig. 3*A*, which shows the dependence of the Lyapunov exponent with parameter c for three different positions and diameters of the hole. The difference between these three curves is a direct consequence of both the pierced hole and the presence of the refractive index. Indeed, when the hole is moved away from the center of the billiard, or its size reduces, the billiard is farther from being symmetric, leading to a higher degree of chaos. In the meantime, areas with a higher refractive index are free from being eliminated and are revealed, further amplifying this difference.

We further inspect the general applicability of quantity $|\boldsymbol{\mu}(r)|$ in *SI Appendix*, section 7 by exploring some other typical SORs and comparing their $|\boldsymbol{\mu}(r)|$ s with the volume of chaotic area in their Poincaré SOSs. The results confirm the universality of $|\boldsymbol{\mu}(r)|$. When the studied objects are generalized from Tannery surfaces to general SORs, different SORs are parameterized by different parameters, and even for SORs that are from the same family, the relation between their parameters and the degree of chaos might not be as simple as it is in Tannery surfaces: that is, where a universal quantity could play a significant role. Another remarkable advantage of defining $|\boldsymbol{\mu}(r)|$ is that given an SOR, one is able to approximately estimate its degree of chaos by simply calculating its $|\boldsymbol{\mu}(r)|$, which can be directly obtained by its metric, instead of investigating more involved signatures of chaos, as we did earlier.

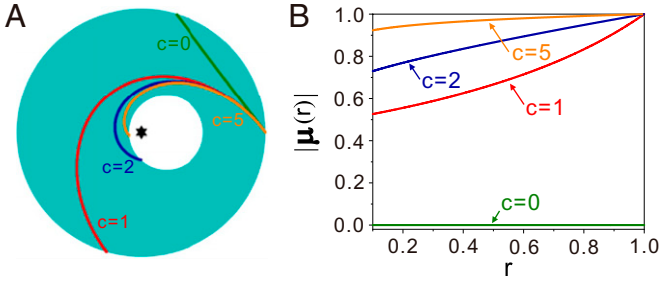

Fig. 5. Fictitious force in projected billiards of Tannery surfaces with different c. (*A*) Comparison of trajectories with the same initial conditions, $\theta = 0$ and $p_\theta = 0.8$, in projected billiards of Tannery surfaces with $c = 0$ (green), 1 (red), 2 (blue), and 5 (orange). The star marks the position of the center of the billiard. (*B*) Comparison of the four surfaces on $|\boldsymbol{\mu}(r)|$, the quantity defined to characterize the degree of trajectories' deflection.

4. Conclusion

In conclusion, we have investigated photonic chaotic dynamics (ray and wave behaviors) on both 3D uniform SORs and in 2D table billiards with a nonuniform refractive index. These two systems are proved to be strictly equivalent for both light rays and waves by applying the idea of a conformal mapping in TO. Such equivalence enables these two different systems to share the same phenomena and serve one another to solve in a simpler manner a complex challenging problem, since a geometry can appear easy and analytical in one system, but untraceable in the other. The present proposal, projecting a 3D SOR onto a nonuniform table

billiard, serves as a practical pathway to help both solve calculation and simulation problems and provide a natural interpretation of the role of curvature in 3D chaotic systems, which probably could be done on the 3D SOR as well, but are much simpler and more straightforward to investigate in the latter. Compared with 3D surfaces, a nonuniform 2D table billiard turns out to be a more promising candidate for experimental design and realization, on account of the difficulty in restricting and controlling lights on the former. Reciprocally, the landscape of the refractive index in nonuniform table billiards can be complex, while transferring it to its corresponding 3D SOR could greatly reduce the parameters. Our investigation also raises an interesting proposal on the design of the refractive index in a nonuniform billiard or cavity to achieve expected features, taking advantage of special trajectories or geometrical properties of its corresponding 3D curved surface. For instance, it is still an open question for how to transfer an arbitrarily deformed chaotic billiard into integrable, by correlating its refractive index profile with an SOR. More underlying physics and potential applications about this system equivalence remain to be explored.

Although we have taken a typical family of SORs, Tannery surfaces, as an example to study the variation of the degrees of chaos in curved space with respect to its control parameter, the model can certainly be generalized to arbitrary SORs. The parameter (curvature)-dependent property of chaotic dynamics on 3D SORs enlightens an efficient and neat mechanism to control and utilize chaos and consequently opens up many perspectives, for example, exploration and control of wave chaos in multimode fiber amplifiers to enhance pump absorption efficiency (61, 62) with nonuniform transverse, or the extensive study of a new type of microcavity (27–30). Furthermore, exploration of chaotic dynamics within the context of non-Euclidean geometry may open a new perspective in studies of chaos in cosmology (63–65).

Data Availability. All study data are included in the article and/or supporting information.

ACKNOWLEDGMENTS. We thank Tsampikos Kottos from Wesleyan University for fruitful discussion on calculation of the Lyapunov exponent; and Kun Tang from Bar-Ilan University for help in COMSOL simulation. C.X. acknowledges the 2019 Israeli "Sandwich Doctorate Program" for international students funded by the Council for Higher Education at Bar-Ilan University. P.S. is thankful for CNRS support under Grant PICS-ALAMO. This research is also supported by The Israel Science Foundation Grants 1871/15, 2074/15, and 2630/20; the United States–Israel Binational Science Foundation NSF/BSF Grant 2015694; Zhejiang Provincial Natural Science Foundation of China Grant LD18A040001; National Natural Science Foundation of China Grants 11674284 and 11974309; and National Key Research and Development Program of China Grant 2017YFA0304202.

Author affiliations: [a]Department of Physics, The Jack and Pearl Resnick Institute for Advanced Technology, Bar-Ilan University, Ramat-Gan 5290002, Israel; and [b]Zhejiang Province Key Laboratory of Quantum Technology and Device, Department of Physics, Zhejiang University, Hangzhou 310027, China

1. K. S. Thorne, R. H. Price, D. A. MacDonald, *Black Holes: The Membrane Paradigm* (Yale University Press, New Haven, CT, 1986).
2. S. Batz, U. Peschel, Linear and nonlinear optics in curved space. *Phys. Rev. A* **78**, 043821 (2008).
3. S. Batz, U. Peschel, Solitons in curved space of constant curvature. *Phys. Rev. A* **81**, 053806 (2010).
4. R. Bekenstein, J. Nemirovsky, I. Kaminer, M. Segev, Shape-preserving accelerating electromagnetic wave packets in curved space. *Phys. Rev. X* **4**, 011038 (2014).
5. E. Lustig *et al.*, Curved-space topological phases in photonic lattices. *Phys. Rev. A* **96**, 041804 (2017).
6. C. Xu, A. Abbas, L.-G. Wang, S.-Y. Zhu, M. S. Zubairy, Wolf effect of partially coherent light fields in two-dimensional curved space. *Phys. Rev. A (Coll. Park)* **97**, 063827 (2018).
7. C. Xu, A. Abbas, L.-G. Wang, Generalization of Wolf effect of light on arbitrary two-dimensional surface of revolution. *Opt. Express* **26**, 33263–33277 (2018).
8. C. Xu, L.-G. Wang, Gouy and spatial-curvature-induced phase shifts of light in two-dimensional curved space. *New J. Phys.* **21**, 113013 (2019).
9. D. Wang, C. Liu, H. Liu, J. Han, S. Zhang, Wave dynamics on toroidal surface. *Opt. Express* **26**, 17820–17829 (2018).
10. H. W. Wu *et al.*, Observation of protected localized states induced by curved space in acoustic topological insulators. arXiv [Preprint] (2021). https://arxiv.org/abs/2101.03294 (Accessed 11 January 2021).
11. V. H. Schultheiss *et al.*, Optics in curved space. *Phys. Rev. Lett.* **105**, 143901 (2010).
12. V. H. Schultheiss, S. Batz, U. Peschel, Hanbury Brown and Twiss measurements in curved space. *Nat. Photonics* **10**, 106–110 (2016).
13. A. Patsyk, M. A. Bandres, R. Bekenstein, M. Segev, Observation of accelerating wave packets in curved space. *Phys. Rev. X* **8**, 011001 (2018).
14. J. Zhu, Y. Liu, Z. Liang, T. Chen, J. Li, Elastic waves in curved space: Mimicking a wormhole. *Phys. Rev. Lett.* **121**, 234301 (2018).
15. R. Bekenstein *et al.*, Control of light by curved space in nanophotonic structures. *Nat. Photonics* **11**, 664–670 (2017).
16. Y. Song *et al.*, Möbius strip microlasers: A testbed for non-Euclidean photonics. *Phys. Rev. Lett.* **127**, 203901 (2021).
17. U. Leonhardt, T. Tyc, Broadband invisibility by non-Euclidean cloaking. *Science* **323**, 110–112 (2009).
18. A. Nicolet, F. Zolla, Physics. Cloaking with curved spaces. *Science* **323**, 46–47 (2009).
19. L. Xu *et al.*, Light rays and waves on geodesic lenses. *Photon. Res.* **7**, 1266–1272 (2019).
20. L. Xu, T. Tyc, H. Chen, Conformal optical devices based on geodesic lenses. *Opt. Express* **27**, 28722–28733 (2019).
21. G. Lefebvre *et al.*, Experiments on Maxwell's fish-eye dynamics in elastic plates. *Appl. Phys. Lett.* **106**, 024101 (2015).
22. P. V. P. Cunha, C. A. R. Herdeiro, E. Radu, Fundamental photon orbits: Black hole shadows and spacetime instabilities. *Phys. Rev. D* **96**, 024039 (2017).
23. A. E. Motter, P. S. Letelier, FRW cosmologies between chaos and integrability. *Phys. Rev. D Part. Fields Gravit. Cosmol.* **65**, 068502 (2008).
24. E. Aydiner, Chaotic universe model. *Sci. Rep.* **8**, 721 (2018).
25. C. Liu *et al.*, Enhanced energy storage in chaotic optical resonators. *Nat. Photonics* **7**, 473–478 (2013).
26. S. Bittner *et al.*, Suppressing spatiotemporal lasing instabilities with wave-chaotic microcavities. *Science* **361**, 1225–1231 (2018).
27. C. Gmachl *et al.*, High-power directional emission from microlasers with chaotic resonators. *Science* **280**, 1556–1564 (1998).
28. J. U. Nöckel, A. D. Stone, Ray and wave chaos in asymmetric resonant optical cavities. *Nature* **385**, 45–47 (1997).
29. M. S. Kurdoglyan, S.-Y. Lee, S. Rim, C.-M. Kim, Unidirectional lasing from a microcavity with a rounded isosceles triangle shape. *Opt. Lett.* **29**, 2758–2760 (2004).
30. J. Wiersig, M. Hentschel, Combining directional light output and ultralow loss in deformed microdisks. *Phys. Rev. Lett.* **100**, 033901 (2008).
31. X. Jiang *et al.*, Chaos-assisted broadband momentum transformation in optical microresonators. *Science* **358**, 344–347 (2017).
32. C. Liu *et al.*, Triggering extreme events at the nanoscale in photonic seas. *Nat. Phys.* **11**, 358–363 (2015).
33. C. Liu, A. Di Falco, A. Fratalocchi, Dicke phase transition with multiple superradiant states in quantum chaotic resonators. *Phys. Rev. X* **4**, 021048 (2014).
34. L. Fan, X. Yan, H. Wang, L. V. Wang, Real-time observation and control of optical chaos. *Sci. Adv.* **7**, eabc8448 (2021).
35. Ya. G. Sinai, On the foundations of the ergodic hypothesis for a dynamical system of statistical mechanics. *Sov. Math Dokl.* **4**, 1818–1822 (1963).
36. M. V. Berry, Regularity and chaos in classical mechanics, illustrated by three deformations of a circular 'billiard'. *Eur. J. Phys.* **2**, 91–102 (1981).
37. L. A. Bunimovich, Mushrooms and other billiards with divided phase space. *Chaos* **11**, 802–808 (2001).
38. D. R. da Costa, C. P. Dettmann, E. D. Leonel, Circular, elliptic and oval billiards in a gravitational field. *Commun. Nonlinear Sci. Numer. Simul.* **22**, 731–746 (2015).
39. M. Robnik, M. V. Berry, Classical billiards in magnetic fields. *J. Phys. Math. Gen.* **18**, 1361–1378 (1985).
40. T. Szeredi, D. A. Goodings, Classical and quantum chaos of the wedge billiard. I. Classical mechanics. *Phys. Rev. E Stat. Phys. Plasmas Fluids Relat. Interdiscip. Topics* **48**, 3518–3528 (1993).
41. Y. Kim *et al.*, Designing whispering gallery modes via transformation optics. *Nat. Photonics* **10**, 647–653 (2016).
42. M. Avlund, C. Ellegaard, M. Oxborrow, T. Guhr, N. Søndergaard, Observation of periodic orbits on curved two-dimensional geometries. *Phys. Rev. Lett.* **104**, 164101 (2010).
43. G. Tanner, N. Søndergaard, Wave chaos in acoustics and elasticity. *J. Phys. A Math. Theor.* **40**, R443–R509 (2007).
44. A. N. Norri, D. A. Rebinsky, Membrane and flexural waves on thin shells. *J. Vib. Acoust.* **116**, 457–467 (1994).
45. D. Wang, C. Liu, S. Zhang, C. T. Chan, Chaotic photon spheres in non-Euclidean billiard. *Nanophotonics* **9**, 3367–3372 (2020).
46. J. B. Pendry, D. Schurig, D. R. Smith, Controlling electromagnetic fields. *Science* **312**, 1780–1782 (2006).
47. D. Schurig *et al.*, Metamaterial electromagnetic cloak at microwave frequencies. *Science* **314**, 977–980 (2006).
48. U. Leonhardt, Optical conformal mapping. *Science* **312**, 1777–1780 (2006).
49. L. Xu, H. Chen, Conformal transformation optics. *Nat. Photonics* **9**, 15–23 (2015).
50. R. D'Inverno, *Introducing Einstein's Relativity* (Oxford University Press, New York, 1992).
51. R. F. Rinehart, A solution of the problem of rapid scanning for radar antennae. *J. Appl. Phys.* **19**, 860–862 (1948).
52. A. L. Besse, *Manifolds All of Whose Geodesics Are Closed* (Springer-Verlag, Berlin, 1978).
53. J. E. Borzellino, C. R. Jordan-Squire, G. C. Petrics, D. M. Sullivan, On the existence of infinitely many closed geodesics on orbifolds of revolution. arXiv [Preprint] (2006). https://arxiv.org/abs/math/0602595 (Accessed 29 June 2019).
54. M. C. Gutzwiller, *Chaos in Classical and Quantum Mechanics* (Springer-Verlag, New York, 1990).
55. G. Datseris, L. Hupe, R. Fleischmann, Estimating Lyapunov exponents in billiards. *Chaos* **29**, 093115 (2019).

56. O. Legrand, F. Mortessagne, "Wave chaos for the Helmholtz equation" in *New Directions in Linear Acoustics and Vibration: Quantum Chaos, Random Matrix Theory and Complexity*, M. Wright, R. Weaver, Eds. (Cambridge University Press, Cambridge, UK, 2010), pp. 24–41.
57. E. J. Heller, Bound-state eigenfunctions of classically chaotic Hamiltonian systems: Scars of periodic orbits. *Phys. Rev. Lett.* **53**, 1515–1518 (1984).
58. T. Zimmermann, H. Meyer, H. Köppel, L. S. Cederbaum, Manifestation of classical chaos in the statistics of quantum energy levels. *Phys. Rev. A Gen. Phys.* **33**, 4334–4341 (1986).
59. E. B. Bogomolny, B. Georgeot, M. Giannoni, C. Schmit, Chaotic billiards generated by arithmetic groups. *Phys. Rev. Lett.* **69**, 1477–1480 (1992).
60. L. A. Bunimovich, Mechanisms of chaos in billiards: Dispersing, defocusing and nothing else. *Nonlinearity* **31**, R78–R92 (2018).
61. L. Philippe *et al*., Experimental study of pump power absorption along rare-earth-doped double clad optical fibres. *Opt. Commun.* **218**, 249–254 (2003).
62. N. A. Mortensen, Air-clad fibers: Pump absorption assisted by chaotic wave dynamics? *Opt. Express* **15**, 8988–8996 (2007).
63. C. Ganguly, M. Bruni, Quasi-isotropic cycles and nonsingular bounces in a mixmaster cosmology. *Phys. Rev. Lett.* **123**, 201301 (2019).
64. A. E. Motter, Relativistic chaos is coordinate invariant. *Phys. Rev. Lett.* **91**, 231101 (2003).
65. N. J. Cornish, E. P. S. Shellard, Chaos in quantum cosmology. *Phys. Rev. Lett.* **81**, 3571–3574 (1998).